Mode-resolved Fabry-Perot experiment in low-loss Bragg-reflection waveguides

B. Pressl,[1*] T. Günthner,[1] K. Laiho,[1] J. Geßler,[2] M. Kamp,[2] S. Höfling,[2,3] C. Schneider,[2] and G. Weihs[1]

[1]*Institut für Experimentalphysik, Universität Innsbruck, Technikerstraße 25, 6020 Innsbruck, Austria*

[2]*Technische Physik, Universität Würzburg, Am Hubland, 97074 Würzburg, Germany*

[3]*School of Physics & Astronomy, University of St Andrews, St Andrews KY16 9SS, United Kingdom*

[*]*Benedikt.Pressl@uibk.ac.at*

Abstract: Based on the interaction between different spatial modes, semiconductor Bragg-reflection waveguides (BRWs) provide a highly functional platform for non-linear optics. For achieving any desired quantum optical functionality, we must control and engineer the properties of each spatial mode. To reach this purpose we extend the Fabry-Perot technique and achieve a detailed linear optical characterization of dispersive multimode semiconductor waveguides. With this efficient broadband spectral method we gain direct experimental access to the relevant modes of our BRWs and determine their group velocities. Furthermore, we show that our waveguides have lower than expected loss coefficients. This renders them suitable for integrated quantum optics applications.

OCIS codes: (070.4790) Spectrum analysis; (130.3120) Integrated optics devices; (130.5990) Semiconductors; (230.7370) Waveguides.

References and links

1. G. I. Stegeman and R. H. Stolen, "Waveguides and fibers for nonlinear optics," J. Opt. Soc. Am. B **6**, 652–662 (1989).
2. M. E. Anderson, M. Beck, M. G. Raymer, and J. D. Bierlein, "Quadrature squeezing with ultrashort pulses in nonlinear-optical waveguides," Opt. Lett. **20**, 620–622 (1995).
3. D. K. Serkland, M. M. Fejer, R. L. Byer, and Y. Yamamoto, "Squeezing in a quasi-phase-matched $LiNbO_3$ waveguide," Opt. Lett. **20**, 1649–1651 (1995).
4. W. Sohler, H. Hu, R. Ricken, V. Quiring, C. Vannahme, H. Herrmann, D. Büchter, S. Reza, W. Grundkötter, S. Orlov, H. Suche, R. Nouroozi, and Y. Min, "Integrated optical devices in lithium niobate," Opt. Photon. News **19**, 24–31 (2008).
5. F. Lederer, G. I. Stegeman, D. N. Christodoulides, G. Assanto, M. Segev, and Y. Silberberg, "Discrete solitons in optics," Phys. Rep. **463**, 1–126 (2008).
6. I. P. Kaminow and L. W. Stulz, "Loss in cleaved Ti-diffused $LiNbO_3$ waveguides," Appl. Phys. Lett. **33**, 62–64 (1978).
7. R. Regener and W. Sohler, "Loss in low-finesse Ti:$LiNbO_3$ optical waveguide resonators," Appl. Phys. B **36**, 143–147 (1985).
8. S. Taebi, M. Khorasaninejad, and S. S. Saini, "Modified Fabry-Perot interferometric method for waveguide loss measurement," Appl. Opt. **47**, 6625–6630 (2008).
9. D. Hofstetter and R. L. Thornton, "Theory of loss measurements of Fabry-Perot resonators by Fourier analysis of the transmission spectrum," Opt. Lett. **22**, 1831–1833 (1997).
10. D. Hofstetter and R. L. Thornton, "Measurement of optical cavity properties in semiconductor lasers by Fourier analysis of the emission spectrum," IEEE J. Quant. Electron. **34**, 1914–1923 (1998).

#249829 Received 9 Sep 2015; revised 30 Oct 2015; accepted 13 Nov 2015; published 21 Dec 2015

11. S. Chen, Q. Yan, Q. Xu, Z. Fan, and J. Liu, "Optical waveguide propagation loss measurement using multiple reflections method," Opt. Comm. **256**, 68–72 (2005).
12. M. Allione, V. V. Temnov, Y. Fedutik, U. Woggon, and M. V. Artemyev, "Surface plasmon mediated interference phenomena in low-q silver nanowire cavities," Nano Lett. **8**, 31–35 (2008).
13. B. J. Bijlani and A. S. Helmy, "Bragg reflection waveguide diode lasers," Opt. Lett. **34**, 3734–3736 (2009).
14. D. B. Anderson and J. T. Boyd, "Wideband CO_2 laser second harmonic generation phase matched in GaAs thin-film waveguides," Appl. Phys. Lett. **19**, 266–268 (1971).
15. M. G. Roelofs, A. Suna, W. Bindloss, and J. D. Bierlein, "Characterization of optical waveguides in $KTiOPO_4$ by second harmonic spectroscopy," J. Appl. Phys. **76**, 4999–5006 (1994).
16. K. Banaszek, A. B. U'Ren, and I. A. Walmsley, "Generation of correlated photons in controlled spatial modes by downconversion in nonlinear waveguides," Opt. Lett. **26**, 1367–1369 (2001).
17. A. D. Rossi, V. Ortiz, M. Calligaro, L. Lanco, S. Ducci, V. Berger, and I. Sagnes, "Measuring propagation loss in a multimode semiconductor waveguide," J. Appl. Phys. **97**, 073105 (2005).
18. P. Abolghasem, J. Han, B. J. Bijlani, A. Arjmand, and A. S. Helmy, "Continuous-wave second harmonic generation in Bragg reflection waveguides," Opt. Express **17**, 9460–9467 (2009).
19. M. Karpinski, C. Radzewicz, and K. Banaszek, "Experimental characterization of three-wave mixing in a multimode nonlinear $KTiOPO_4$ waveguide," Appl. Phys. Lett. **94**, 181105 (2009).
20. A. Christ, K. Laiho, A. Eckstein, T. Lauckner, P. J. Mosley, and C. Silberhorn, "Spatial modes in waveguided parametric downconversion," Phys. Rev. A **80**, 033829 (2009).
21. P. J. Mosley, A. Christ, A. Eckstein, and C. Silberhorn, "Direct measurement of the spatial-spectral structure of waveguided parametric down-conversion," Phys. Rev. Lett. **103**, 233901 (2009).
22. R. Machulka, J.Svozilik, J. Soubusta, J. Perina, and O. Haderka, "Spatial and spectral properties of fields generated by pulsed second-harmonic generation in a periodically poled potassium-titanyl-phosphate waveguide," Phys. Rev. A **87**, 013836 (2013).
23. J. D. Bierlein, A. Ferretti, L. H. Brixner, and W. Y. Hsu, "Fabrication and characterization of optical waveguides in $KTiOPO_4$," Appl. Phys. Lett. **50**, 1216–1218 (1987).
24. M. Fiorentino, S. M. Spillane, R. G. Beausoleil, T. D. Roberts, P. Battle, and M. W. Munro, "Spontaneous parametric down-conversion in periodicall poled KTP waveguides and bulk crystals," Opt. Express **15**, 7479–7488 (2007).
25. A. Helmy, P. Abolghasem, J. S. Aitchison, B. Bijlani, J. Han, B. Holmes, D. Hutchings, U. Younis, and S. Wagner, "Recent advances in phase matching of second-order nonlinearities in monolithic semiconductor waveguides," Laser Photon. Rev. **5**, 272–286 (2011).
26. A. Valles, M. Hendrych, J. Svozilik, R. Machulka, P. Abolghasem, D. Kang, B. J. Bijlani, A. S. Helmy, and J. P. Torres, "Generation of polarization-entangled photon pairs in a Bragg reflection waveguide," Opt. Express **21**, 10841–10849 (2013).
27. J. J. Wathen, P. Apiratikul, C. J. K. Richardson, G. A. Porkolab, G. M. Carter, and T. E. Murphy, "Efficient continuous-wave four-wave mixing in bandgap-engineered AlGaAs waveguides," Opt. Lett. **39**, 3161–3164 (2014).
28. L. Lanco, S. Ducci, J.-P. Likforman, X. Marcadet, J. A. W. van Houwelingen, H. Zbinden, G. Leo, and V. Berger, "Semiconductor waveguide source of counterpropagating twin photons," Phys. Rev. Lett. **97**, 173901 (2006).
29. R. Horn, P. Abolghasem, B. J. Bijlani, D. Kang, A. S. Helmy, and G. Weihs, "Monolithic source of photon pairs," Phys. Rev. Lett. **108**, 153605 (2012).
30. D. Menashe, M. Tur, and Y. Danziger, "Interferometric technique for measuring dispersion of high order modes in optical fibres," Electron. Lett. **37**, 1439–1440 (2001).
31. J. W. Nicholson, A. D. Yablon, S. Ramachandran, and S. Ghalmi, "Spatially and spectrally resolved imaging of modal content in large-mode-area fibers," Opt. Express **16**, 7233–7243 (2008).
32. T. Günthner, B. Pressl, K. Laiho, J. Geßler, S. Höfling, M. Kamp, C. Schneider, and G. Weihs, "Broadband indistinguishability from bright parametric downconversion in a semiconductor waveguide," J. Opt. **17**, 125201 (2015).
33. P. Abolghasem, J. Han, B. J. Bijlani, A. Arjmand, and A. S. Helmy, "Highly efficient second-harmonic generation in monolithic matching layer enhanced $Al_xGa_{1-x}As$ Bragg reflection waveguides," IEEE Photon. Technol. Lett. **21**, 1462–1464 (2009).
34. C. M. Herzinger, C. C. Lu, T. A. DeTemple, and W. C. Chew, "The semiconductor waveguide facet reflectivity problem," IEEE J. Quant. Electron. **29**, 2273–2281 (1993).
35. D. E. Aspnes, S. M. Kelso, R. A. Logan, and R. Bhat, "Optical properties of AlxGa1-xAs," J. Appl. Phys. **60**, 754–767 (1986).
36. A. Yariv and P. Yeh, *Photonics* (Oxford University, 2007), 6th ed.
37. A. E. Siegman, *Lasers* (University Science Books, 1986).
38. S. Gehrsitz, F. K. Reinhart, C. Gourgon, N. Herres, A. Vonlanthen, and H. Sigg, "The refractive index of $Al_xGa_{1-x}As$ below the band gap: Accurate determination and empirical modeling," J. Appl. Phys. **87**, 7825–7837 (2000).
39. Princeton Instruments Spectroscopy Group, "Fully automated wavelength calibration method optimizes data

#249829 Received 9 Sep 2015; revised 30 Oct 2015; accepted 13 Nov 2015; published 21 Dec 2015

accuracy," (2011).
40. K. Liu and F. Yu, "Accurate wavelength calibration method using system parameters for grating spectrometers," Opt. Eng. **52**, 013603 (2013).
41. P. Jansson, *Deconvolution of Images and Spectra* (Academic Press, 1997).
42. W. Guo, Y. Huang, C. Han, and L. Yu, "Measurement of gain spectrum for Fabry-Perot semiconductor lasers by the Fourier transform method with a deconvolution process," IEEE J. Quant. Electron. **39**, 716–721 (2003).

1. Introduction

Waveguided light sources are widely employed in many applications both in the field of classical and quantum optics, since the light inside them can simultaneously be guided very flexibly and controlled strictly [1–5]. The confined waveguide size results in a finite selection of transversal modes that can propagate through the structure, further determining whether only a single optical mode is supported or if a multitude of them is accepted.

The linear optical waveguide characteristics such as refractive index and its dispersion, transmission losses or the reflectivity at the end facets are relevant to practical purposes and important feedback for manufacturing. One often employed loss measurement technique is the Fabry-Perot characterization that is suitable for structures with well-cleaved, parallel end facets that have at least modest reflectivity [6]. After travelling several round trips inside the waveguide light interferes, and fringes can be observed in the transmission if the optical length the light sees inside the resonator is changed for example by heating it [7] or by altering the wavelength of light [8]. The loss characteristics can then be extracted from the fringe contrast. In the latter case this information can also be extracted via the Fourier transformation of the transmission spectrum [9]. With this technique, properties of sophisticated structures such as single-mode semiconductor lasers, surface plasmon resonators and ridge waveguides have been investigated and indications of cavity defects have been observed [10–13].

Regarding waveguides, their typically very rich spatial mode structure [14–16] may pose a significant challenge in their application. For single mode waveguides a clear fringe contrast can be recorded in the Fabry-Perot transmission. However, for multimode waveguides this is not the case [17, 18]. Nevertheless, the mode-resolved characteristics are of great interest, especially for non-linear optical waveguides that are utilized as frequency-converted photon sources. Thus, the characteristics of all interacting modes have to be carefully studied for optimizing the conversion processes [19–22]. Despite sophisticated fabrication techniques, single-mode waveguides that have a non-linear optical response are challenging to manufacture and multimodeness is often introduced in the fabrication process by the chosen waveguide shape and size [22–24]. The multimodeness can also be taken advantage of, as is the case in Bragg-reflection waveguides (BRWs) that are built from semiconductor compounds [25]. The mode structure of BRWs is highly complex, and apart from supporting the total-internal-reflection modes they also carry higher-order modes, such as the Bragg modes [26]. This is necessary for their use in frequency conversion processes. Recent demonstrations show that semiconductor waveguides are a versatile source for four-wave mixing [27] and parametric down-conversion (PDC) [28, 29].

Here, we present an extension of the existing Fabry-Perot technique of linear optical characterization for transversally multimode waveguides and apply this method to our BRWs. Similar to measurements of the group delay difference in multimode fibers [30, 31], our analysis uses the fact that different spatial modes generally possess different dispersion. In our case, however, the system allows for a direct and highly accurate determination of the absolute group effective indices. These parameters play an important role, for example, in the PDC process [28, 29, 32]. The applied method gives access to the loss characteristics in a mode resolved manner. Our results show a low level of total loss in the Bragg mode and excellent uniformity across several samples. Additionally, we extract a lower bound for the number of excited modes and estimate

#249829 Received 9 Sep 2015; revised 30 Oct 2015; accepted 13 Nov 2015; published 21 Dec 2015

the strength of the light coupling for the desired modes. By investigating waveguides with different cross-sections we show that the multimodeness is increasing with a larger waveguide size.

2. Theoretical Background

BRWs are well-suited for loss measurements via the Fabry-Perot technique, due to the high refractive index (>3) of the semiconductor material. If their facets are uncoated, typically a Fresnel reflectivity of about 30% is expected. Thus, the waveguide forms a low-finesse ($\mathscr{F} \approx 2.5$) Fabry-Perot resonator. The transmission spectrum of this resonator can be readily calculated by summation of the complex field amplitudes at the facets. Following the notation in [9], the transmittance of this resonator in terms of a vacuum wavenumber $\beta = 2\pi/\lambda$, where λ is the vacuum wavelength of the light, is given by

$$T(\beta) = \frac{(1-R)^2 \exp(-2kL\beta) + 4\sin(\phi)}{[1-R\exp(-2kL\beta)]^2 + 4R\exp(-2kL\beta)\sin^2(\phi + nL\beta)}, \tag{1}$$

where L is the physical length of the resonator (i.e. waveguide length), R and ϕ are the reflectivity and phase change at the facet, respectively. In the dispersive case, the frequency-dependent effective index of the mode $n = n(\beta)$ can be substituted. Linear losses are modeled through a complex effective index $\tilde{n} = n + ik$, where k is the absorption index that can be related to the linear loss coefficient α via the vacuum wavelength λ_0 with $k = \frac{\alpha\lambda_0}{4\pi}$. The Fourier-transformed transmission spectrum shows distinct peaks centered at integer multiples of the optical length $n_g L$ of the dispersive resonator, with n_g being the group index of the mode. As the light propagates through the waveguide it accumulates some phase. In terms of the Fourier transform a phase shift in real space causes a translation in Fourier space. Consequently, the individual facet reflections are separated in the Fourier domain, with the amplitude at each reflection being preserved. Thus, the *ratio of the amplitudes* of subsequent peaks indicates the total loss $\widetilde{R}$ at each pass, which is given by

$$\widetilde{R} = Re^{-\alpha L}. \tag{2}$$

If R and L are known, calculating α is straightforward.

The linearity of the Fourier transform is a key feature for applying the Fabry-Perot analysis to multimode waveguides. Essentially, individual Fabry-Perot resonators are formed for the different modes with their differing group effective indices. This is justified if the sample is designed in a way that avoids interaction between the orthogonal eigenmodes [17]. To facilitate this constraint in our BRWs, the cross-section of the waveguides along the propagation direction remains constant and adjacent waveguides are isolated by separating them far enough so that evanescent coupling is avoided. Usually the spacing of modes in the effective index scale is narrow, and therefore, complex beating effects are recorded in the transmission spectrum. However, the distinct propagation indices lead to distinct optical lengths, and hence, it is possible to observe and measure each mode individually in Fourier space. In addition to this the relative excitation strength of each mode is also preserved.

Strictly speaking, the "multimode inverse Fabry-Perot transform" is an ill-posed inverse problem as the number of contributing modes is not known a-priori. The Fourier transform is not the proper inverse, but it simplifies the problem enough to enable modally resolved measurements. Note that system-dependent additional effects, for example limited spectral resolution, may influence the Fourier transform. Thus, the achievable measurement accuracy will vary depending on the studied waveguide and its optical properties. Furthermore, the Fourier method will take the collective data into account instead of just the minima and maxima of fringe contrast, which makes it more robust against noise. Simulations are useful for understanding the

#249829 Received 9 Sep 2015; revised 30 Oct 2015; accepted 13 Nov 2015; published 21 Dec 2015

implications these effects on the measurements (see Appendix A). Figure 1 shows a simulation of the expected spectrum of a two-mode system representative of our sample. Due to the uncertainty principle, measuring several dozens of fringes is required to get a high resolution mode spectrum in Fourier space. Nevertheless, a lot of information can already be gained by visual inspection and interpretation, since reading the spectrum is easy and intuitive.

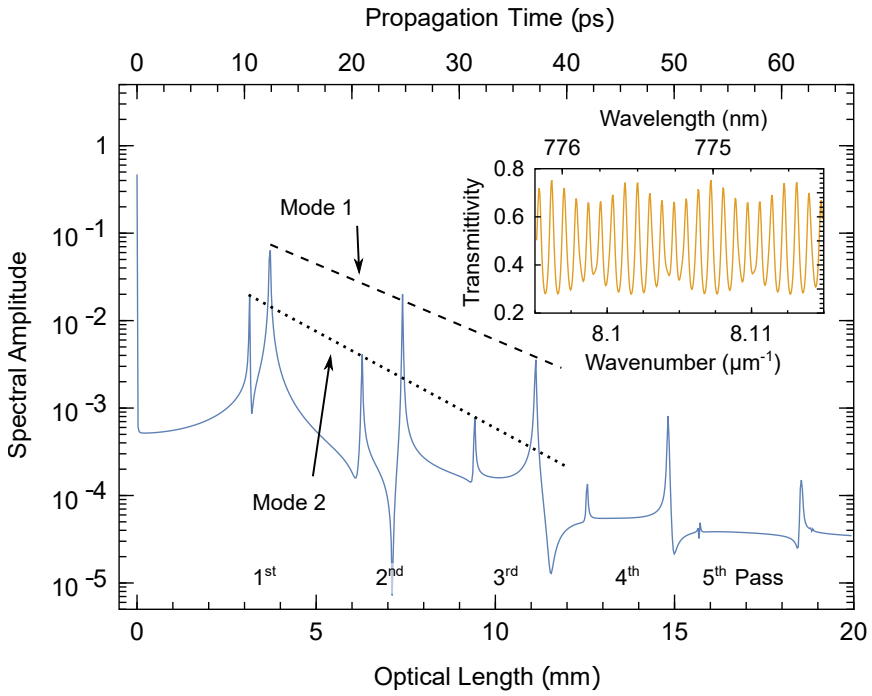

Fig. 1. Simulated spectrum of the fringe pattern of two dispersive ($n_{g,1} = 4.1$, $n_{g,2} = 3.5$) and lossy modes ($R = 0.3$, $k = 10^{-5}$) representative of our 0.9 mm long sample. Excitation strength is 80% for Mode 1 and 20% for Mode 2. The peaks appear at multiples of the resonators optical lengths indicating the group effective index for each mode. There are five passes of each mode visible. The inset shows an excerpt of the simulated fringe pattern with its two-mode beating.

3. Experiment

We are interested in the BRW properties in the near infrared region around 780 nm, since the Bragg mode in this wavelength regime is exploited to pump the process of PDC [32]. Our BRWs are fabricated with molecular beam epitaxy and have the layer structure described in [29, 33]. The ridges are defined by electron beam lithography and transferred into the semiconductor via reactive plasma etching (see Fig. 2). We investigate BRW samples with two different lengths, 0.9 mm and 2.0 mm, which are cleaved pieces of a larger sample. Ridge widths from 3.0 to 6.5 μm in 0.5 μm steps were used. Our BRWs are modally phase matched for nonlinear conversion processes between the NIR and telecom range.

In our experiment as illustrated in Fig. 3(a), we launch the broadband light of a superluminescent diode (SLED, Superlum BLMS mini, centered at 777 nm, 17.4 nm FWHM) with power and polarization control into our BRW with a 100× microscope objective. The polarization of the input beam is kept horizontal. After the waveguide the transmitted light is collimated with

#249829 Received 9 Sep 2015; revised 30 Oct 2015; accepted 13 Nov 2015; published 21 Dec 2015

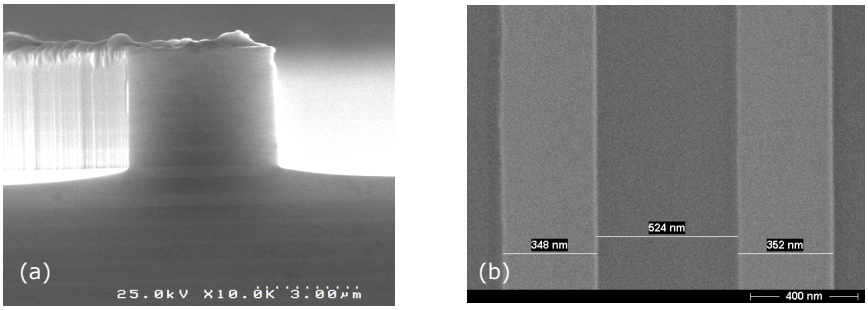

Fig. 2. SEM image of a waveguide on the sample. (a) The ridge after carrying out the measurements. Note that the sample has been exposed to the laboratory atmosphere for more than half a year. (b) Close view of the core region. The SEM-measured thickness values were used in the detailed simulation in Appendix B.

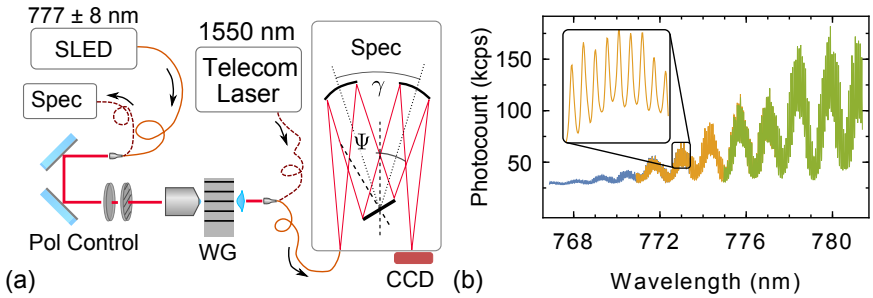

Fig. 3. (a) Experimental setup consisting of the SLED, polarization control optics (half-wave plate and sheet polarizer), coupling optics (microscope objective and aspheric lens) and spectrograph. For optimization on SHG (see main text), a tunable telecom laser is back-coupled and analyzed with another spectrometer. Ψ and γ are the geometrical parameters of the spectrograph used for calibration (see Appendix C). (b) Raw, 14.5 nm wide, stitched transmission spectrum where different colors show the three exposures of different wavelength ranges. The 210 Fabry-Perot fringes of the waveguide resonator are superimposed on the oscillation (FSR $\approx$ 2 nm) of another resonator formed by other optics. The power envelope is determined by the spectrum of the SLED.

an aspheric lens and coupled to a single-mode fiber. The single-mode fiber may cut out some modes or affect their coupling strengths, this is, however, a prerequisite for gaining the desired resolution. Nevertheless, in this configuration our measurement technique provides direct indication to what extent higher order modes can be coupled to or excited via a single mode fiber. The collected light is then directed through an spectrograph incorporating a grating with a 1800 grooves/mm (Acton SP2750 with 750 mm focal length), where we image the end facet of the single mode fiber onto a 2D camera with large sensor and small pixels (9×9 µm^2, SBIG STT-1603ME). The achievable spectral resolution with this setup is better than 10 pm FWHM across the entire image plane. Figure 3(b) shows a typical transmissions spectrum of our waveguides. In general, we employ two different procedures to optimize coupling into the waveguide: either maximizing the transmitted intensity, which causes most power to be coupled to the TIR mode, or using a more elaborate scheme that involves second-harmonic generation (SHG). In the latter case, we couple a telecom laser backwards for generating second harmonic light at NIR in the phase-matched Bragg-mode. Since the light of the second-harmonic is only in the Bragg mode, we can easily optimize the coupling of this mode to the single mode fiber.

#249829 Received 9 Sep 2015; revised 30 Oct 2015; accepted 13 Nov 2015; published 21 Dec 2015

4. Results

Our results in Fig. 4(a) illustrate two different measurement configurations. First, we only optimize the transmission through the waveguide into the single mode fiber. In this case, shown as a blue solid line in Fig. 4(a), most of the input light couples to the fundamental total internal reflection (TIR) mode. After SHG optimization (yellow solid line in Fig. 4(a)) we can easily identify the Bragg-mode and clearly notice that the amount of light coupled into the Bragg mode is largely increased, while the other peaks corresponding to other modes stay approximately the same. We note that, while most of the power is still coupled to other modes, the amplitude of the Bragg-mode is increased twofold. By integrating over the spectrum of the first pass, we estimate that in the SHG optimized case 8% of the in-coupled power is guided by the Bragg-mode. Furthermore, in Fig. 4(b) five excited modes can be identified for the given waveguide. As each mode has a different group index, we can separate the modes from the background by searching for a signal at twice the optical length. Figure 4(c) shows the number of clearly identifiable modes with respect to the ridge width (see also Appendix B). These values are only lower bounds on the minimum number of excited modes because closely spaced or degenerate modes cannot be separated. Nevertheless, a clear trend is visible that the number of modes increases with increasing ridge width.

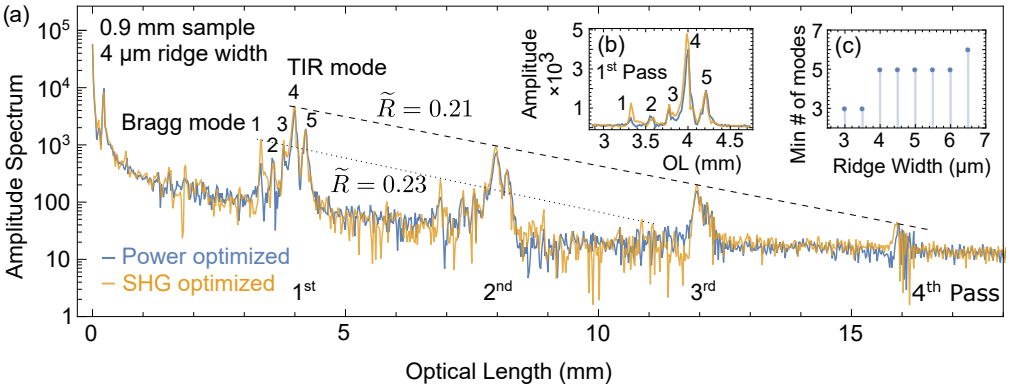

Fig. 4. (a) Modulus of the Fourier transform of the transmission spectrum from Fig. 3(b) (blue solid line). Superimposed is a second spectrum showing the result from optimizing by maximizing SHG in the waveguide (orange solid line). The strongest mode is visible up to the 4th pass. Two modes and their respective total loss value $\widetilde{R}$ are indicated. (b) Linear plot of the first pass with five easily discernible modes. (c) The minimum visible mode numbers of several waveguides with different ridge widths.

In order to determine the mode loss, Eq. (2) has to be employed. Since only $\widetilde{R}$ and L are known, we are left with two unknowns: the modal reflectivity R and the loss value α. We have two samples with different lengths (0.9 mm and 2.0 mm) but identical waveguides available. If we rewrite Eq. (2) as a function of L, $\widetilde{R}(L) = Re^{-\alpha L}$ we can find a least-squares solution for α and R simultaneously. In order to get good statistics, we measure multiple similar waveguides at each of the two waveguide lengths. Both values strongly depend on the exact value of $\widetilde{R}$, so corrections for the limited resolution have to be applied (see Appendix D). For our BRWs, we retrieve a TIR mode reflectivity of $R = 0.35(4)$ and an ensemble loss coefficient of $\alpha = 0.5(1)\,\mathrm{mm}^{-1} = 2.2(5)\,\mathrm{dB/mm}$. The expected Fresnel reflectivity is 0.30 for an interface between a material with refractive index of 3.4 and air. However, the Fresnel equations tend to underestimate the semiconductor waveguide facet reflectivity. For systems similar to ours, we may say that the mode reflectivity is 20 % higher than the Fresnel reflectivity [34]. This is in

#249829 Received 9 Sep 2015; revised 30 Oct 2015; accepted 13 Nov 2015; published 21 Dec 2015

good agreement with the measured value.

For the modes of the waveguide in Fig. 4, taking the values of $\widetilde{R}$ and the facet reflectivity of $R = 0.35(4)$, yields linear loss coefficients of $\alpha_{\mathrm{TIR}} = 0.46(12)\,\mathrm{mm}^{-1}$ and $\alpha_{\mathrm{Bragg}} = 0.36(12)\,\mathrm{mm}^{-1}$. A survey of many waveguides with different ridge widths indicates that total loss $\widetilde{R}$ varies only about 10% for both modes. This suggests a high quality, highly repeatable waveguide fabrication and a lower level of loss than previously reported for BRW modes [13, 29].

These values are much higher than expected from numerical simulations (see also Appendix B), which take into account mainly the leakage of the mode through the Bragg mirrors. Other potential loss mechanisms are material absorption and scattering through imperfections and side-wall roughness along the waveguides. Absorption losses reported for the material with the highest loss ($Al_{0.2}Ga_{0.8}As$) [35] are two orders of magnitude smaller than the measured linear loss coefficient. Thus, scattering because of side-wall roughness and imperfections seem to be the main loss mechanism.

Finally, by investigating the location of the peaks in Fig. 4(a) on the optical length scale we can estimate the group indices. This yields group velocities of $v_g^{\mathrm{TIR}} = 68(1)\,\mu\mathrm{m/ps}$ and $v_g^{\mathrm{Bragg}} = 81(1)\,\mu\mathrm{m/ps}$ for the TIR and Bragg modes at the NIR, respectively. Additionally, in Fig. 5 we show a dispersion map similar to a spectrogram. Analyzing the transmission spectrum in limited wavelength ranges allows us to trace a change in the group index with changing wavelength. The resulting map hints at the group velocity dispersion (GVD) of each individual mode.

Being highly sensitive to the slope of the dispersion characteristic, the group velocity and GVD delivers an accurate test of the used dispersion model (see Appendix B). From our results, we also conclude that the in the NIR the Bragg mode lies below the respective TIR mode in the group index scale, and has a lower GVD. Other than that, these parameters are crucial, for example, for modelling the joint spectral properties of the twin photons created in the process of PDC. For BRWs these values are typically gained from numerical simulations (see [32] and references therein). Luckily, for highly dispersive resonators, the Fourier analysis provides direct experimental access and a starting point for more detailed analyses.

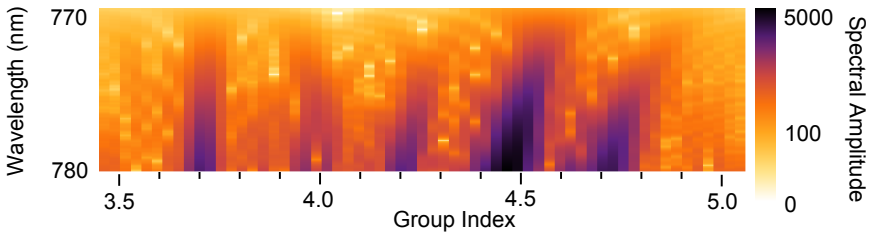

Fig. 5. Dispersion map, or spectrogram, of the first pass of the waveguide in Fig. 4. Each horizontal row represents a mode spectrum like Fig. 4, but only a limited wavelength range of the original transmission spectrum data is processed. Each part is weighted with a sinc window and centered on the wavelength plotted on the vertical axis. The window is then slightly shifted on the wavelength axis and the resulting slices are stacked. This allows a more local recovery of the group index at the expense of resolution in the mode spectrum. A mode-dependent shift of the group index with the central wavelength of the window is clearly visible, indicating GVD.

#249829 Received 9 Sep 2015; revised 30 Oct 2015; accepted 13 Nov 2015; published 21 Dec 2015

5. Conclusion

To summarize, we have shown how Fourier analysis of the optical transmission spectrum can provide useful information about the modal structure of multimode waveguides. We have applied this method to our BRW samples at NIR wavelengths, where their rich modal structure prevent the fringe contrast method from providing sufficient data. From our results we can infer the linear characteristics in a mode resolved manner and illustrate the mode spectrum of a low-loss BRW sample. Our technique, especially when combined with broadband spectroscopy, can be employed towards multimode waveguide characterization in many integrated optics platforms.

A. Transmission spectrum: simulation and analysis

The transmission spectrum of a simple, isolated ridge waveguide is determined by its reflectivity of the air interface and the phase shift accumulated along the propagation direction. In that sense, the waveguide forms a Fabry-Perot resonator, with the transmitted light showing the interference of partial reflections accumulated through multiple round-trips. The transmission spectrum shows a series of distinct Lorentzian peaks, whose width is determined by the coefficient of finesse and, subsequently, through the reflectivity. The position of the peaks is determined by the single-pass phase

$$\delta(\beta) = n(\beta) L \beta, \tag{3}$$

where L is the waveguide length, $\beta = 2\pi/\lambda$ is the vacuum wavenumber of the mode and n(β) is the dispersive effective index of the mode.

As motivated in section 2, assuming orthogonal modes [17] the total multimode spectrum can be calculated as the sum of multiple resonators' spectra as

$$I(\beta) = \sum_n x_i T_i(\beta), \tag{4}$$

in which x_i denotes the amount of light coupled to the i-th mode.

In Eq. (5) , the normalized transmission spectrum of the i-th single Fabry-Perot cavity is given by

$$T_i(\beta) = \frac{(1-R_i)^2 \exp(-2k_i L\beta) + 4\sin(\phi)}{[1-R_i \exp(-2k_i L\beta)]^2 + 4R_i \exp(-2k_i L\beta)\sin^2(\phi + \delta_i(\beta))}, \tag{5}$$

where k is the absorption index and R and ϕ are the facet reflectivity and the corresponding phase shift. The Fresnel equations provide good initial estimates of the reflectivity $R = \left[(n-1)^2 + k^2\right] / \left[(n+1)^2 + k^2\right]$ and phase shift $\phi = \arctan\left[-2k/(n^2+k^2-1)\right]$. In the limit of very low loss $k \ll n$, however, the phase shift ϕ can be neglected. For a certain mode i, we assume only that the phase accumulated along the propagation direction $\delta_i(\beta)$ changes according to the effective index of the mode $n_i(\beta)$. Furthermore, we note that in the dispersive case, the spacing of the peaks in frequency domain, or free spectral range (FSR), is effectively given by the group index $n_g = n + \omega \frac{\partial n}{\partial \omega}$, with ω being the angular frequency of the light [36, 37]. This result carries on to the Fourier domain: the "optical length" measured from the peak position of each mode actually reports $n_g L$ in first approximation . The GVD may cause an additional broadening of the peaks (see Fig. 7).

To simulate the measurement of the spectrometer, $I(\beta)$ is sampled in frequency space according to the pixel spacing of our spectrometer camera. The result is Gaussian filtered with a filter width equivalent to the measured resolution of the spectrometer (see Section D). Subsequent

#249829 Received 9 Sep 2015; revised 30 Oct 2015; accepted 13 Nov 2015; published 21 Dec 2015

simulations show that the power variation of the utilized broadband light source (superluminescent diode) has little effect on the higher-order peaks appearing at multiple resonator passes, aside from slightly reducing the signal.

B. Comparing the mode spectrum with extended simulations

For a more detailed qualitative investigation of BRW's spatial and spectral dispersion properties we use numerical simulations to interpret the results in (Figs. 4 and 5). These simulations require certain additional parameters which strongly affect the result: an exact model of the refractive index of the $Al_xGa_{1-x}As$ system is required and the layer thicknesses and waveguide lengths have to be measured. Then, a mode solver (Mathematica 10.2, COMSOL 5.0) is used to determine the effective index of certain modes in the wavelength range between 760 nm and 790 nm. The total multimode transmission spectrum is then calculated from the individual modes according to Eqs. 4 and 5 using the same values for the absorption index k and the modal reflectivity R as in Fig. 1. Subsequent analysis of the transmission spectrum is then carried out analogous to the experiment.

The simulated group indices of the relevant modes and their respective shapes are seen in Fig. 6. For sake of simplicity, the simulations are carried out in a 1D slab configuration. Since the waveguides are relatively wide (> 3 µm), the dispersive properties of the modes are mostly determined by the dispersion of the materials.

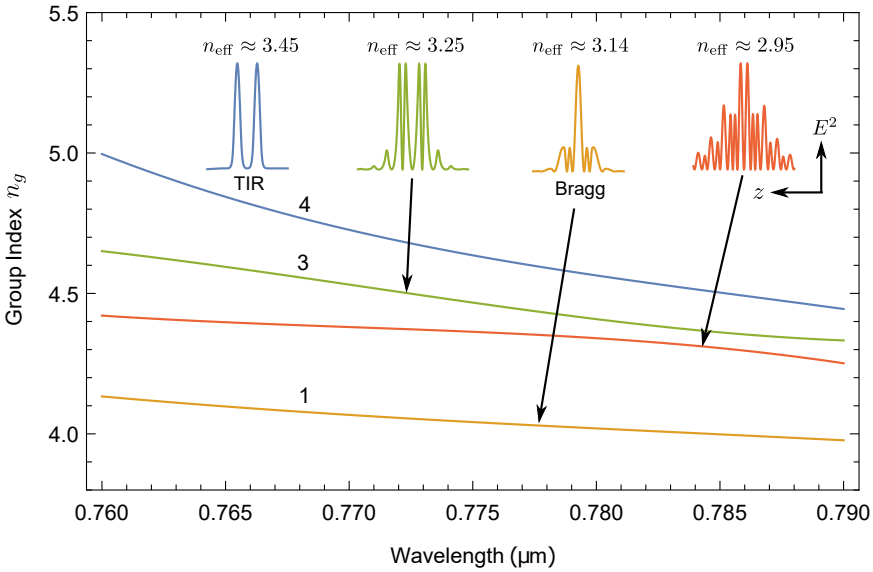

Fig. 6. Group indices of the four simulated slab modes with their respective mode shape E^2 along the vertical direction z. We do not expect the lowest effective index mode to contribute significantly to the spectrum. Nevertheless, this illustrates that the group index can be drastically different than the effective index. The numbers indicate the corresponding modes in Fig. 4. Intuitively, we expect the TIR mode to be the strongest mode, while the Bragg mode can be identified by the SHG optimization procedure (see Sec. 3). Furthermore, the simulated group index dispersion as well as the relative separation to the TIR and Bragg modes match best for mode 3 in Figs. 4 and 5.

When comparing the simulation in Fig. 6 to our experimental results in Figs. 4 and 5, we notice that the 1D simulations account for three of the five observed modes. We believe the other two modes are defined by the finite extension of the ridge, where horizontal confinement

#249829 Received 9 Sep 2015; revised 30 Oct 2015; accepted 13 Nov 2015; published 21 Dec 2015

needs to be taken into account. In 2D simulations, the complex structure of the BRW ridge causes the appearance of thousands of spurious modes, which make a full survey of the dispersion very challenging. While these modes are in principle solutions to the wave equation in the simulation, they are, however, not relevant in practice. Examples include highly radiative modes propagating at the absorptive boundary of the simulation or modes propagating along the surface or the substrate.

As expected, we find the Bragg-mode at a lower group index than the TIR mode. However, the simulated group indices are consistently shifted by 0.3 when compared to the experiment. We attribute this to the accuracy of the refractive index model employed [38]. Despite utilizing a high precision dispersion model, the seemingly high difference is still well within the uncertainty of the model. This is because the group index is highly sensitive to slope of the refractive index. If the slope of the model is slightly different than in the experiment, a constant shift is introduced. Note that other possible sources of errors, like varying layer thicknesses or aluminum concentrations also affect the group index, but the combined, worst-case effect is less than 10 % of the observed deviation.

Further simulations have shown that the group index measured is highly stable with respect to any accountable systematic error, like calibration (see Appendices C and D). Therefore, the measured group index can be taken as very reliable and thus serve as a test for the refractive index model. For example, one can think of adding corrections to the refractive index model to better represent the sample.

Finally, Fig. 7 shows the result of the Fourier analysis of the simulated multimode transmission spectrum including the three modes found in Fig. 6. In addition to the slight shift of the expected optical lengths, one can clearly see the broadening of the mode peaks compared to Fig. 4. This broadening is caused by the GVD of the modes and, subsequently, the refractive index model. Similar to the group index, the refractive index model seems to overestimate the GVD, but also within the uncertainty of the model. To conclude, we find a good qualitative agreement between the experiment and simulation.

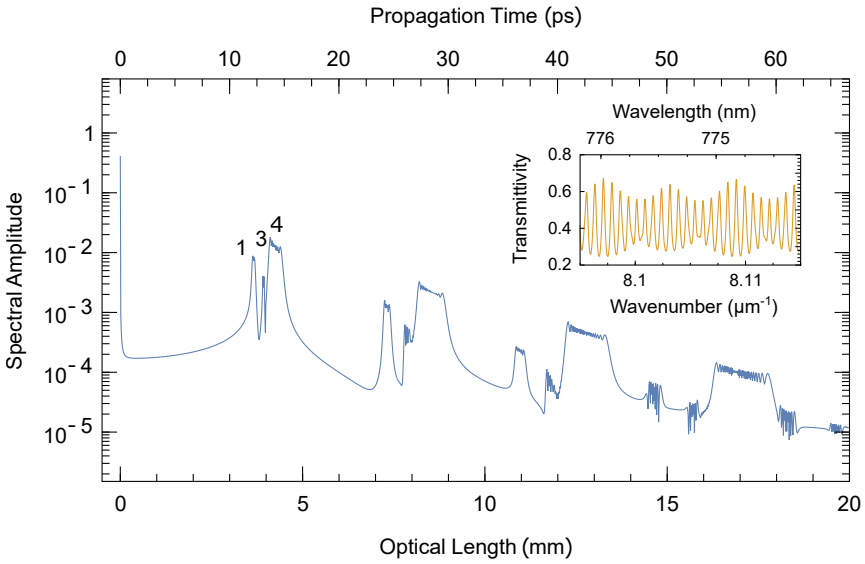

Fig. 7. Fourier mode spectrum with four simulated modes, and three easily discernible. The inset shows a portion of the simulated multimode transmission spectrum. The numbers indicate the corresponding modes in Fig. 4.

#249829 Received 9 Sep 2015; revised 30 Oct 2015; accepted 13 Nov 2015; published 21 Dec 2015

C. Spectrograph considerations

The FSR of the waveguide resonator scales inversely proportional to the group index and resonator length. Therefore, care has to be taken when using a spectrograph for recording the fringes, especially with regard to the resolution. The Lorentzian aspect of the peaks and the beating pattern has to be properly resolved.

In our case, the group indices of the waveguide eigenmodes lie between 3.1 and 4.1, which leads to a free spectral range of only 40 pm for a 2 mm long sample. Also, in order to record more fringes, several exposures at different central wavelengths have to be stitched together. A modified Czerny-Turner model [39] was used as calibration function, as the higher order polynomial model performed unsatisfactorily due to the large spacing of the lines in this wavelength range. The calibration model relates the observed wavelength λ at the pixel position Δx_{cam} for a given "central wavelength" setting λ_c of the spectrometer controller:

$$\begin{aligned}\lambda(\Psi,\Delta x_{\mathrm{cam}}) = \frac{d}{m}\Bigg[&\sin\left(\Psi-\frac{\gamma}{2}-\arctan\frac{\Delta x_{\mathrm{in}}}{f}\right)\\ &+\sin\left(\Psi+\frac{\gamma}{2}+\arctan\frac{\Delta x_{\mathrm{cam}}}{f}\right)\Bigg], \text{ and}\\ \Psi(\lambda_c) = \arcsin&\left(\frac{m\lambda_c}{2d\cos\frac{\gamma}{2}}\right).\end{aligned} \tag{6}$$

Equation (6) is based on the key geometrical parameters of the spectrograph (see also Fig. 8): γ is the inclusion angle between grating and the mirrors, Ψ is the grating angle calculated from λ_c, the diffraction order m and the groove spacing d of the grating. Δx_{in} and Δx_{cam} are the off-center distances of the input fiber and camera, respectively. During the measurement, only the central wavelength λ_c was changed.

The calibration and resolution measurement was done by investigating several lines of a low-pressure Argon lamp between 763 and 801 nm (see Fig. 9). These bright Argon lines served as reference for a total of 110 different (λ_c, Δx_{cam}) pairs. Despite having few emission lines around 775 nm, the typical calibration error is less than 10 pm in the wavelength region of interest. This is more then enough to do a pixel-accurate stitch of three spectra with ≈ 6.5 nm coverage each and an overlap of ≈ 2.4 nm. This yields a total spectrum of 14.5 nm showing approximately 210 (0.9 mm length sample, see main text Fig. 1) to 350 (2.0 mm length) fringes.

We note, that any nonlinearity on the wavelength calibration results in an artificial "dispersion", as there is an additional, frequency-dependent scaling error. The previously stated calibration error of 10 pm over 14.5 nm yields a nonlinearity of 0.07 %. In comparison, the refractive index of the weakest dispersive material in our system, $Al_{0.8}Ga_{0.2}As$, changes approximately by 0.2 % in the same wavelength range.

The use of geometrical model of the spectrograph with the addition of Δx_{in} as extra parameter is critical in achieving the required calibration accuracy. However, more intricate geometrical models, for example with a ray optics approach, show that there is still some room for improvement [40].

D. Correcting for limited resolution

The finite resolution of the spectrograph affects the values of the total loss $\widetilde{R}$, so here we show a simple correction scheme for this parameter. Recovery can be performed by recognising that limited resolution simply biases $\widetilde{R}$ towards lower values deterministically, depending on the group index of the mode and the resolution of the spectrometer. This is motivated by the properties of the Fourier transform: the recorded transmission spectrum is convolved with the point-

#249829 Received 9 Sep 2015; revised 30 Oct 2015; accepted 13 Nov 2015; published 21 Dec 2015

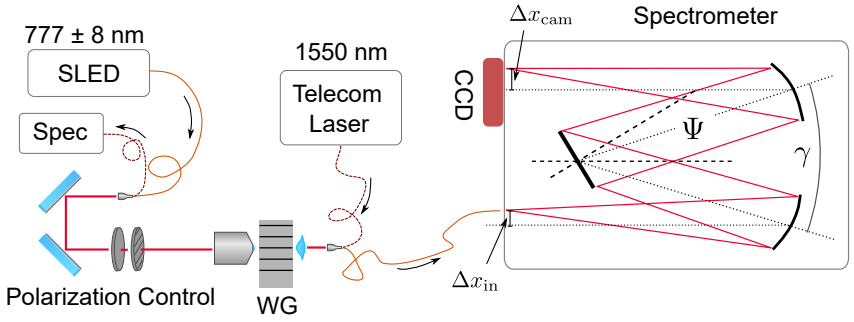

Fig. 8. Experimental setup for recording the transmission spectrum. Note that Δx_{in} is strongly exaggerated for illustration purposes.

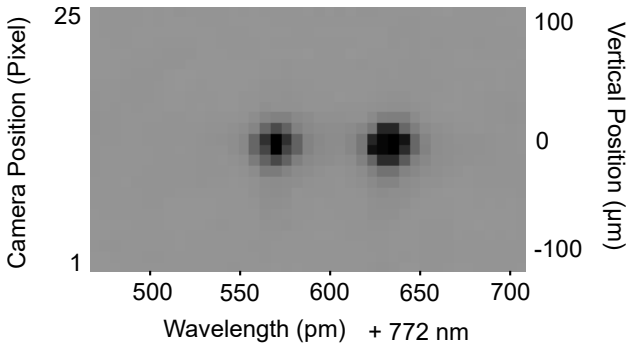

Fig. 9. Real space camera image of the Argon 772.5887 nm and 772.6333 nm lines.

spread function (PSF) of the spectrograph (see Fig. 9). For the sake of simplicity, we assume that the PSF can be represented as a narrow Gaussian whose width corresponds to the resolution. The individual pixels of the CCD can be seen a dirac comb which is convolved with the PSF to model the instrument response. In Fourier space, the convolution becomes a multiplication and the narrow Gaussian of the PSF transforms to a wide Gaussian with a width inversely proportional to the resolution. The multiplication of the Fourier transformed signal with the wide Gaussian causes damping at high optical lengths. This results in lower than expected values for $\widetilde{R}$. In that sense, the uncorrected loss values should be seen as upper bound.

Figure 10 shows correction curves for four modes with different group indices in the range expected in our sample. The corrected $\widetilde{R}$ is simply calculated by multiplying the measured value with the correction factor for a given waveguide length and group index. In the case of the 0.9 mm length sample discussed in the main text, the raw total loss values are expected to be overstated by about 10 % on average. For the long, 2.0 mm length samples, it may be as high as 60 % with our setup.

A more elaborate method is deconvolving the original transmission spectrum, which is a well-studied technique in spectroscopy [41]. This approach has also been discussed in the context of the Fabry-Perot problem in microlaser gain measurements [42], but care has to be taken in order to preserve the signal-to-noise ratio and avoid the introduction of artifacts.

#249829 Received 9 Sep 2015; revised 30 Oct 2015; accepted 13 Nov 2015; published 21 Dec 2015

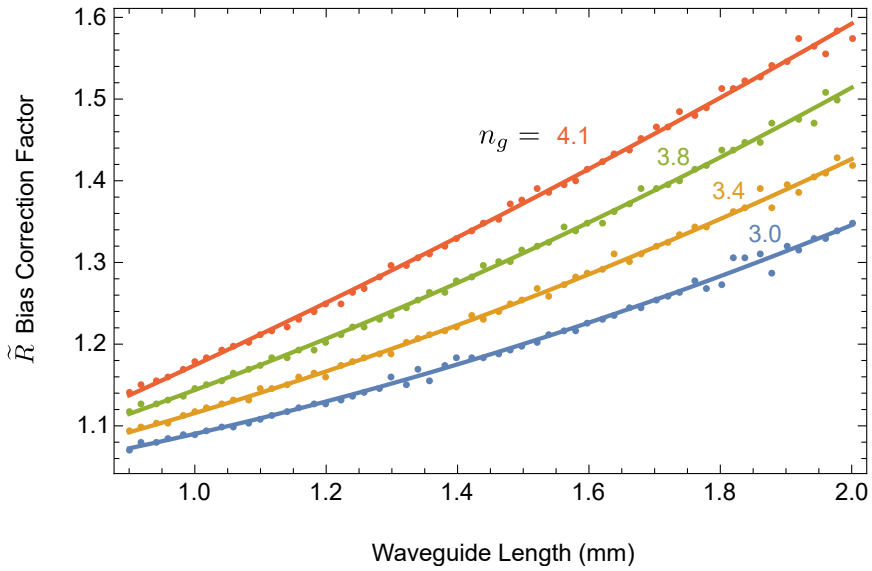

Fig. 10. Bias of the total loss $\widetilde{R}$ for several modes with different group indices for the resolution (10 pm) measured in our system. For example, with a 0.9 mm sample the measured values of $\widetilde{R}$ may be multiplied with a correction factor of $1.07 - 1.14$, depending on the mode.

Acknowledgements

This work was supported by the FWF project no. I-2065-N27, the DFG Project no. SCHN1376/1-1 and the ERC project *EnSeNa* (257531).

We thank M. Sassermann and Z. Vörös for laboratory assistance and A. Sailer for technical support.

#249829 Received 9 Sep 2015; revised 30 Oct 2015; accepted 13 Nov 2015; published 21 Dec 2015